Final Draft
of the original manuscript:

Size effects in short fibre reinforced composites

I. Scheider[1], Y. Chen[1], A. Hinz[1], N. Huber[1], J. Mosler[1,2]*

[1]*Helmholtz-Zentrum Geesthacht, Institute of Materials Research, Materials Mechanics, Geesthacht, Germany*
[2]*TU Dortmund, Institute of Mechanics, D-44227 Dortmund, Germany.*

*corr. author: joern.mosler@hzg.de

Abstract

The present paper is concerned with the analysis of size effects in short fibre reinforced composites. The microstructure of such composites often represents the first hierarchy level of a bioinspired material. For modelling fibre cracking as well as debonding between fibre and matrix material, a fully three-dimensional cohesive zone model is applied. It is shown that this model indeed captures the size effect associated with material failure of a single fibre. Furthermore, this scaling effect strongly depends on the shape and orientation of the assumed pre-existing crack. For this reason, a two-dimensional description can usually only predict the size effect qualitatively. Based on the aforementioned findings, a representative volume element (RVE) containing ceramic fibres embedded within a polymer matrix is considered. Similar to the single fibre, the RVE also shows a pronounced size effect. However, the underlying physical process is significantly more complex. More explicitly, the size effect of the RVE is a superposition of that related to the isolated fibres as well as of that induced by debonding of the fibres from the matrix material. For estimating the different effects, a perfect bond is also modelled.

Keywords: Composites; Size effect; short fibre; cohesive zone model; debonding

1. Introduction

High performance materials typically possess a microstructure which is optimized for the applied loading conditions. The probably most impressive examples can be found in nature. Among those are the biomaterials wood and bone, see e.g. [1][2][3][4]. A well known man-made class of materials mimicking to some extent biomaterials are fibre reinforced composites, cf. [1]. Such composites show a very promising strength to weight ratio and thus, they are already frequently used in the aerospace industry - for instance, in the new airbus A380. Although understanding material failure of fibre reinforced composites is thus of utmost importance, many questions in this area remain unanswered.

Clearly, failure of fibre reinforced composites depends on the mechanical properties of the underlying constituents being fibres and the matrix. In this regard, cracking of the fibres and/or the matrix has to be mentioned. Furthermore, the interaction between the different materials plays also an important role. A typical example is given by debonding of the fibres embedded within the surrounding matrix material. A representative collection of failure mechanisms which can be observed in fibre reinforced composites is given in [5]. One of the most relevant and consequently most often investigated issues in failure assessment of such composites is the competition between fibre breaking and debonding. Usually, material selection and processing parameters are chosen such that debonding is not observed. Analytical investigations on the competition between debonding and breaking are given, e.g. in [6], while experimental observations of these failure mechanisms are presented in [7].

According to the previous paragraph, the overall macroscopic mechanical response of fibre reinforced composites is very complex. That holds in particular for the resulting failure mechanism defining the macroscopic strength of such materials. For this reason, designing fibre reinforced composites having improved fracture properties is by no means straightforward.

The aforementioned optimization can be tackled by at least two different approaches. The first of those, and probably the most intuitive one, is the variation of the involved constituents. Alternatively, the geometry of the fibres can be modified. At a first glance, the second option is not that obvious. However, failure in fibre reinforced composites and that of the underlying constituents is strongly size dependent. Accordingly, the strength of such composites can be significantly influenced by a variation of the fibres' diameter and length. The quantification of this size effect is precisely the subject addressed in the present paper.

A relatively simple analytical model for understanding the aforementioned size effects was recently given by Gao and co-workers, cf. [2]. Within the cited work, the authors investigated the flaw tolerance of

biological composites. According to their model, the size effect of such composites is mostly defined by that of the fibres. This size effect, in turn, depends strongly on the diameter of the fibres, cf. [8]. Without going into detail here, Gao and co-workers showed that the classical Dugdale–Barenblatt model as well as Griffith's theory predict that a pre-existing crack does not propagate below the theoretical strength, if the diameter of the respective fibre is smaller than a certain threshold. Typically, that threshold is of the order of several nanometres. The analytical model by Gao and co-workers is closely related to earlier works presented by Carpinteri [9], who proposed a brittleness number for assessing the failure behaviour of structures.

Although the aforementioned models do capture the size effect in fibre reinforced composites qualitatively, they are based on rather crude approximations. For instance, the model presented in [2] is strictly speaking one-dimensional, the assumed constitutive models (Dugdale–Barenblatt model as well as Griffith) cannot be applied to arbitrary composites and the complex debonding mechanism of the fibres is not considered accurately. Furthermore, the imperfection of the fibres is modelled by a pre-existing symmetric centre crack. In summary, it is not clear under which circumstances the model [2] captures the size effect also quantitatively. However, that is important for designing novel materials that are supposed to combine improved strength and fracture toughness properties.

In the present paper and inspired by the papers [2], [8] and [9], the size effect of composites is investigated by suitable numerical models capable of representing local effects in more detail. An overview of existing models is given in [10]. Among these approaches, cohesive models have been proven to be very useful in particular for capturing debonding between different materials, see e.g. [11] for particle debonding, or [12] for a composite. The competing failure mechanisms of fibre breaking and debonding have also been investigated by using cohesive models since the early 1990's in the pioneering works by Tvergaard, see e.g. [13], see also [14] and [15]. A three-dimensional model focusing on crack bridging and debonding effects induced by the fibres was presented in [16].

In the present paper, the size effect associated with material failure of fibre reinforced composites is numerically investigated by fully three-dimensional representative volume. In line with the models discussed in the previous paragraph, fibre cracking and debonding of the fibres are captured by using a cohesive zone model.

The present paper is organized as follows: The foundations of the constitutive models required for the numerical analysis of fibre reinforced composites are given in Section 2. Focus is on cohesive zone models for fibre cracking and debonding. Inspired by [2], that model is subsequently applied in Section 3 to a size effect study of a single fibre. In extension to [2], the influence of the shape and orientation of the pre-existing crack is also quantified. Finally, the size effect of composites is investigated in Section 4. For that purpose, a representative volume element made of periodic unidirectionally oriented fibres is considered and numerically analyzed.

2. Constitutive assumptions – Cohesive zone models

The constitutive models used within the present paper are briefly described in this section. While the mechanical response of the bulk material before material failure is captured by using standard local continuum approaches, cracks and slip bands are approximated by cohesive zone models. Such models go back to the pioneering works [17] by Dugdale for ductile materials and [18] by Barenblatt for brittle materials. They have been introduced within the framework of the finite element method by Hillerborg and co-workers, cf. [19].

Within cohesive zone models, the stress vector T_s acting at a yet not fully open crack is postulated to be a function depending on the displacement discontinuity $[\![u]\!]$, i.e. the crack opening. A sketch of that idea is given in Fig. 1.
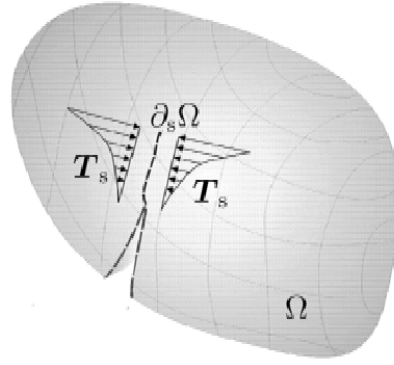
Fig. 1. Modelling material failure by means of a cohesive zone approach. The traction vector $\boldsymbol{T}_s$ is a monotonically decreasing function depending on the displacement discontinuity (amplitude) $[\![\boldsymbol{u}]\!]$. A fully open crack is stress-free, i.e. $\boldsymbol{T}_s = \boldsymbol{0}$.

Denoting the displacement field on the left hand side of the crack as $\boldsymbol{u}^-$ and that on the right hand side as $\boldsymbol{u}^+$, the displacement discontinuity $[\![\boldsymbol{u}]\!]$, also known as the *displacement jump*, is introduced as

$$[\![\boldsymbol{u}]\!] := \boldsymbol{u}^+ - \boldsymbol{u}^- \tag{1}$$

In contrast to classical local continuum models relating the strain tensor to the stress tensor, cohesive zone models are based on a traction separation law of the type

$$\boldsymbol{T}_s = \boldsymbol{T}_s([\![\boldsymbol{u}]\!]) \tag{2}$$

From a continuum mechanical point of view, Eq. (2) defines the response of a so-called *Cauchy elastic material*. It is well known that such a material model can violate the second law of thermodynamics. More precisely, Eq. (2) can usually not be derived from a potential.

Potential-based cohesive zone models were originally advocated by Needlemann and co-workers, cf. [20] and [21]. A review of these approaches can be found in [22]. However, as shown in [23] the existence of a potential is only a necessary condition for thermodynamical consistency. In line with the framework presented in [23], a simple cohesive zone model fulfilling the dissipation inequality is presented here. It is based on damage mechanics and it is derived by applying the by now classical Coleman & Noll procedure, cf. [24]. For a thermodynamically consistent model suitable for the analysis of localized plastic deformation, the interested reader is referred to [25].

Following [26], the Helmholtz energy

$$\Psi([\![\boldsymbol{u}]\!], d) = (1 - d)\, \Psi_0([\![\boldsymbol{u}]\!]) \tag{3}$$

of the cohesive zone model is assumed. Here, $d \in [0; 1]$ is a scalar-valued damage parameter. While the virgin material is characterized by $d = 0$, a fully open stress-free macro-crack is signalled by $d = 1$. According to Eq. (3), Ψ_0 is the stored energy associated with the undamaged material. In what follows, an isotropic response is considered here. Accordingly, Ψ_0 depends on the displacement jump only through its amplitude, i.e.

$$\Psi_0 = \Psi_0(\|\,[\![\boldsymbol{u}]\!]\,\|) \tag{4}$$

For the sake of simplicity, the quadratic energy functional

$$\Psi_0 = \frac{1}{2}\, c\, \|\,[\![\boldsymbol{u}]\!]\,\|^2 \tag{5}$$

is considered within the numerical examples. Here, the material parameter c is the (penalty) initial stiffness of the cohesive interface.

With the aforementioned assumptions, the Coleman & Noll procedure can be applied. For that purpose, the dissipation inequality

$$\mathcal{D} = \boldsymbol{T}_s \cdot [\![\dot{\boldsymbol{u}}]\!] - \dot{\Psi} = \left[\boldsymbol{T}_s - \frac{\partial \Psi}{\partial [\![\boldsymbol{u}]\!]}\right] \cdot [\![\dot{\boldsymbol{u}}]\!] + \Psi_0\,\dot{d} \geq 0 \tag{6}$$

is computed. Consequently, considering a reversible state ($\dot{d} = 0$, $\mathcal{D} = 0$) yields the stress response

$$\boldsymbol{T}_{\mathrm{s}} = (1 - d)\,\frac{\partial \Psi_0}{\partial \|[\![\boldsymbol{u}]\!]\|}\,\frac{[\![\boldsymbol{u}]\!]}{\|[\![\boldsymbol{u}]\!]\|} = (1 - d)\,c\,[\![\boldsymbol{u}]\!] \tag{7}$$

As a result of the assumed isotropy of Ψ_0, the stress vector $\boldsymbol{T}_s$ is parallel to the displacement jump $[\![\boldsymbol{u}]\!]$. Finally, by inserting Eq. (7) into Eq. (6), the reduced dissipation inequality

$$\mathcal{D} = \Psi_0\,\dot{d} \geq 0 \tag{8}$$

is derived. Since $\Psi_0 \geq 0$, Eq. (8) implies that damage has to increase monotonically. Physically speaking, Eq. (8) means that a crack can only grow, while self-healing is prohibited.

The constitutive model is completed by suitable evolution equations for the damage variable d. As evident from Eq. (8), the energetically dual variable of d is the stored energy Ψ_0 of the virgin material. For this reason, thermodynamics suggests an evolution equation of the type $d = d(\Psi_0)$. However, since Ψ_0 is not necessarily monotonic, such an equation would violate the second law of thermodynamics. Therefore, the monotonically increasing internal variable κ is introduced and damage evolution is postulated by

$$d_{n+1} = d(\kappa_{n+1}) \qquad \kappa(t_{n+1}) = \max\{\kappa_n;\,\Psi_0(\|[\![\boldsymbol{u}]\!]_{n+1}\|)\} \qquad \kappa(t = 0) = \kappa_0 \tag{9}$$

In Eq. (9), $(\bullet)_n$ and $(\bullet)_{n+1}$ are variables associated with the pseudo times t_n and t_{n+1}, respectively. According to Eq. (8) and Eq. (9), if $d(\kappa) \in [0;1]$ is monotonically increasing, the second law of thermodynamics is automatically fulfilled.

For defining the presented constitutive model, the material parameters c, κ_0 and the function $d(\kappa)$ are required. Clearly, the initial stiffness c can be interpreted as a penalty parameter und thus, it has simply to be chosen as sufficiently large. By way of contrast, κ_0 defines the elastic limit. If $\|[\![\boldsymbol{u}]\!]\| \leq \sqrt{2\,\kappa_0/c}$, the state is fully elastic. Otherwise, a dissipative process occurs. In this case, damage evolution is driven by the monotonically increasing function $d(\kappa)$. Its shape corresponds to the underlying failure mode, cf. [23]. Furthermore, the respective material parameters have to be chosen such that the fracture energy

$$\mathcal{G}_f := \int_{t=0}^{t_{\mathrm{failure}}} \boldsymbol{T} \cdot \mathrm{d}\,[\![\boldsymbol{u}]\!] = \underbrace{\int_{t_0}^{t_{\mathrm{failure}}} \dot{\Psi}\,\mathrm{d}t}_{=0} + \int_{d=0}^{d=1} \Psi_0\,\mathrm{d}d = \underbrace{\Psi_0\,d\big|_{t_0}^{t_{\mathrm{failure}}}}_{=\kappa_{\mathrm{failure}}} - \int_{\kappa_0}^{\kappa_{\mathrm{failure}}} d(\kappa)\,\mathrm{d}\kappa \tag{10}$$

of the considered material is met.

Remark: Damage accumulation under compression is avoided by replacing $\kappa_{n+1} = \max\{\kappa_n;\,\Psi_0\}$ by

$$\kappa_{n+1} = \max\{\kappa_n;\,\tilde{\Psi}_0\}, \qquad \tilde{\Psi}_0 = \frac{1}{2}\,c\,\|[\![\boldsymbol{u}]\!] + [\langle[\![\boldsymbol{u}]\!] \cdot \boldsymbol{n}\rangle - ([\![\boldsymbol{u}]\!] \cdot \boldsymbol{n})]\,\boldsymbol{n}\|^2 \tag{11}$$

In Eq. (11), $\langle\bullet\rangle$ denotes the Macaulay brackets, i.e. $\langle X\rangle = X$, if $X \geq 0$, while $\langle X\rangle = 0$, if $X < 0$. Thus, mode-I separation is only active for tension.

3. Size effect for precracked fibres

3.1. Fundamentals

In structural failure assessment, tearing of flawed components is typically characterized by general fracture hypotheses such as those of linear elastic fracture mechanics (LEFM). The limits of LEFM are reached when plasticity occurs to a larger extent or when the flaw is very small compared to the characteristic length of the considered components. While in the first case, LEFM has to be replaced by elastic-plastic fracture mechanics, limit load analysis can be used in the latter case. Characteristic

parameters for defining the range of application corresponding to the different aforementioned approaches have been developed by several authors, e.g. by Hillerborg [19] and by Carpinteri [9]. Gao et al. [8] investigated the limits of LEFM for small sized specimens in the range of micrometers or below. Based on a thorough study of crack initiation based on the Dugdale model [17], they stated that a structure of size h smaller than a value given by

$$h \leq \frac{\mathcal{G}_f E}{\sigma_c^2} =: h_{ft} \tag{12}$$

has the intrinsic capability to tolerate crack-like flaws of all sizes, and hence the (micro-)structure was then called 'flaw-tolerant'. The variable E is the Young's modulus and $\sigma_c = \max\left(|\boldsymbol{T_s}|\right)$ is the maximum strength of the material. Assuming a homogeneous and uniaxial stress state, Eq. (12) can be derived by considering the analytical solution of a centre cracked or double edge cracked plate. The size limit of flaw-tolerant structures is denoted as h_{ft}.

Since Eq. (12) is based on rather crude approximations (one-dimensional model, Dugdale–Barenblatt model or Griffith's model, debonding of fibres not considered, ...), the objective of the present paper is to verify this equation also for other types of pre-existing cracks by more precise fully three-dimensional constitutive models. Furthermore, it will be evaluated whether this simple analytically derived equation can also be applied to polymer composites.

In all numerical analyses, the damage variable d in Eq. (9) is defined such that a linear softening in terms of $|\boldsymbol{T}\left(\llbracket\boldsymbol{u}\rrbracket\right)|$ occurs after damage initiation, i.e. the maximum stress σ_c is reached at the point of damage initiation. Furthermore, total failure is assumed, when the separation reaches its critical value δ_c. Accordingly, $d = 1$ at that point. δ_c can be calculated from the cohesive strength and energy by $\delta_c = 2\mathcal{G}_f/\sigma_c$. The cohesive stiffness c is chosen such that damage initiation occurs at approximately 1% of the critical separation.

Before damage initiation, the material is modelled by Hooke's law with material parameters taken from [25]. The material parameters are summarized in Tab. 1 and represent reasonable choices for ceramic fibres. It bears emphasis that the material parameters do not correspond to a pure ceramic but can be understood as obtained from a homogenization of a lower scale. Therefore the cohesive strength is lower than that of real ceramics. The same holds for the fracture energy, which is larger than that of pure ceramics.

Tab. 1: Material parameters characterizing ceramic fibres.

Young's modulus	E	250,000 MPa
Poisson's ratio	ν	0.27
Fracture energy	$\mathcal{G}_f$	640 J/m^2
Cohesive strength	σ_c	600 MPa
Cohesive elastic stiffness	c	50,000 MPa/µm
Critical separation	δ_c	1.067 µm
flaw tolerant size	h_{ft}	440 µm

3.2. Validation of the model by Gao et al. [8]: Numerical modeling of a precracked ceramic strip

Gao et al. [8] stated that a structure of size less than h_{ft} can sustain flaws of any size up to the ultimate strength of the material. This statement is checked here by more accurate finite element simulations. The specimen under consideration is a flat plate of width $2W$ with centre crack (size $2a_0$). Its height H is five times larger than the width of the specimen and the length of the initial crack is 10% of the specimen's width. Due to symmetry, only one quarter of the structure is considered within the finite element simulations and the stress state is approximated by plane stress conditions. Within all simulations, a geometrically equivalent spatial discretization consisting of 225 cohesive elements and 3800 continuum elements (8300 degrees of freedom) has been used. The ligament region of the specimen is shown in Fig. 2.
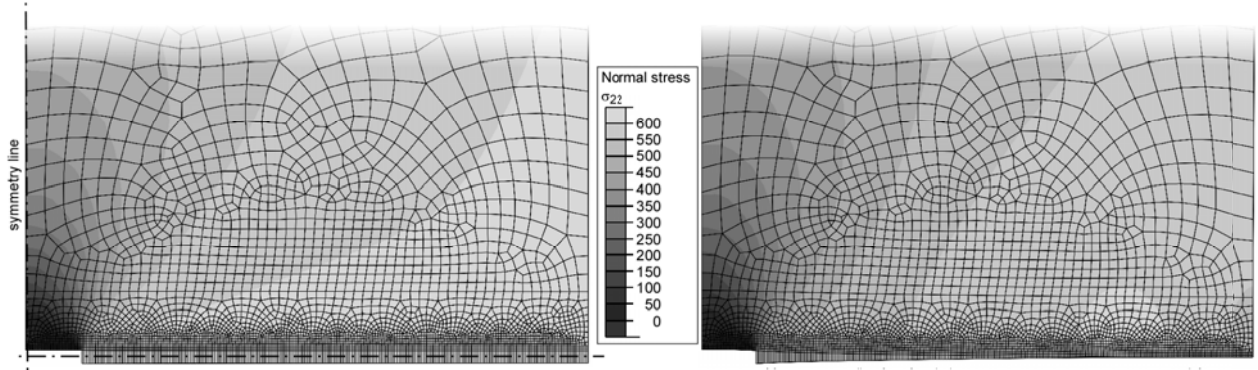
Fig. 2: Detail of the deformed 2D cracked specimens (double symmetry is utilized); a) small specimen ($W = 1$ µm) showing an almost homogeneous crack opening; b) large specimen ($W = 600$ µm) showing a pronounced opening at the crack tip.

The simulations have been performed for sizes in the range of $W = [0.05 \ldots 4000]$ µm. The predicted peak stress σ_{peak}, calculated as force divided by ligament area, divided by the cohesive strength, σ_c, is shown in Fig. 3a. From the graph it can be seen that the curve has a horizontal asymptote for specimen sizes approaching zero. For sizes significantly larger than h_{ft}, the peak stress decreases linearly in the logarithmic diagram. Within the intermediate region, the slope changes gradually. The horizontal asymptote observed for sufficiently small specimens and an extrapolation of the linear decreasing slope for large specimens cross almost exactly at the limit value of $h_{ft} = 440$ µm calculated from Eq. (12). The predicted macroscopic fracture energy as a function in terms of the specimen size looks similar: The normalized fracture is 1.0 within an accuracy of 99% until the threshold defined by Eq. (12) is reached. Subsequently, the fracture energy decreases. The curvature within the transition zone between the aforementioned regimes is significantly higher for the fracture energy compared to the peak stress.

The reason for the decreasing peak stress can be explained by Fig. 2: For the small specimen shown in Fig. 2a, the cohesive strength is reached simultaneously in the whole ligament, i.e., no stress concentration at the crack tip exists, while for the larger specimen (Fig. 2b), a pronounced crack tip region is formed. Although the back end of the specimen has not even reached the maximum stress level, the crack tip elements are already in the softening regime, and hence the average value over the whole ligament never reaches the cohesive strength.
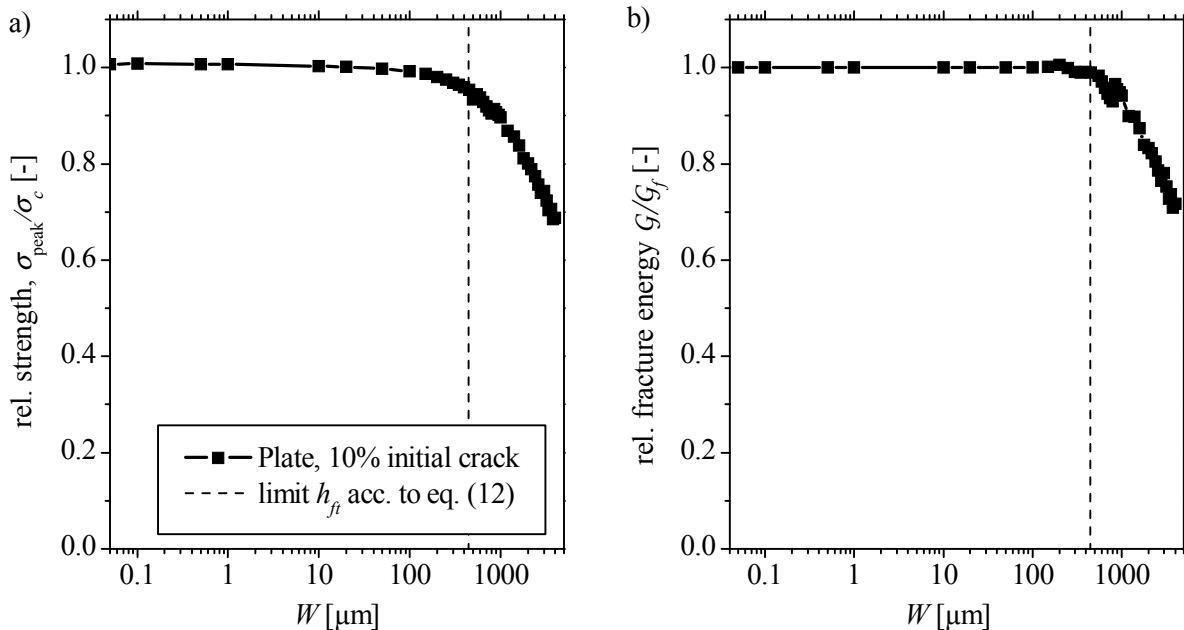

Fig. 3: Size effect of 2D cracked specimens (initial crack width 10% of the specimen's width; threshold proposed by Gao et al. [8] is also shown; see Eq. (12)): a) Peak stress normalized by cohesive strength; b) fracture energy normalized by cohesive energy.

3.3. 3D Modeling of a precracked fibre – Influence of the pre-existing crack's shape

Next, the threshold proposed by Gao and co-workers (see Eq. (12)) is re-analyzed by means of fully three-dimensional finite element simulations. Conceptually, the same procedure as discussed in the previous subsection is applied. More precisely, geometrically equivalent fibres with different radii ranging from 0.05 μm to 1000 μm are considered. In contrast to Subsection 3.2, a surface cracked fibre is investigated in addition to a centre cracked one. The area of that crack is assumed to be 10% of that of the whole fibre. The finite element model of the specimen having a centre crack and that showing a surface crack is significantly different: While for a centre cracked fibre an axisymmetric model similar to that shown in Fig. 2 is sufficient, a fully three-dimensional model must be used for capturing the surface cracked fibre as shown in Fig. 4. The crack front radius for the latter is assumed to be equal to the fibre's radius. Again, the finite element mesh is the same for all different sizes with 38000 continuum and 1400 cohesive elements resulting in 130500 degrees of freedom.
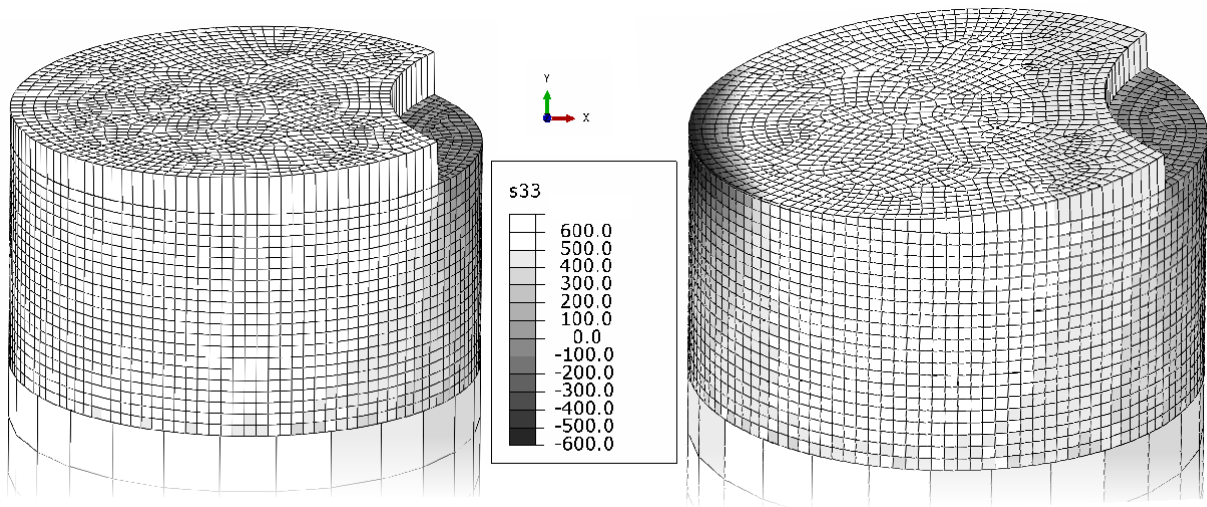

Fig. 4: Deformed 3D edge cracked fibre. a) small diameter (2 μm) showing an almost homogeneous crack opening; b) large diameter (40 μm) showing a pronounced opening at the crack tip and compressive stress at the back face.

As in the previous section, the peak stress and the fracture energy have been determined with respect to the size of the structure. The results for both crack configurations are shown in Fig. 5.

On the one hand, the curves for the centre cracked model look very similar to those for the flat specimens in Fig. 3. Again, a constant peak stress for small radii and a gradually decreasing stress above the limit introduced by Gao and co-workers can be observed. A similar curve is also predicted for the cohesive energy.

On the other hand, the peak stress for the surface cracked fibre decreases already for much smaller specimens. For R = 5 μm, the peak stress is already 7% lower than the cohesive strength. However, the energy is constant until R = 20 μm. Only for even larger specimens, it also decreases. The reason for the different size effect of the surface cracked fibre is twofold:

1. The surface crack promotes bending in the fibre due to the unsymmetric ligament area.
2. The curved crack front leads to a non-constant crack driving force along the front. For instance, at the edges, which discover a higher load due to the bending, the damage rate is higher, i.e., they will fail first.

Both effects are not independent but strongly affect each other: When damage occurs at the crack tips at the edges of the specimen, the resulting non-constant distribution of the stresses leads to even more pronounced bending effects which, in turn, result in larger loading of the crack tip. This effect is visible in Fig. 4. While for the small fibre with R = 1 μm (Fig. 4a) the stress and the opening of all cohesive elements is similar, a completely different scenario can be seen for the fibre with R = 20 μm (Fig. 4b): Even though this size is far below the limit proposed by Gao and co-workers, bending is so pronounced that the compressive stresses at the back side of the ligament are of similar magnitude as the tensile stresses. Therefore, crack opening can only be seen at the crack tip with highest values at the edges.
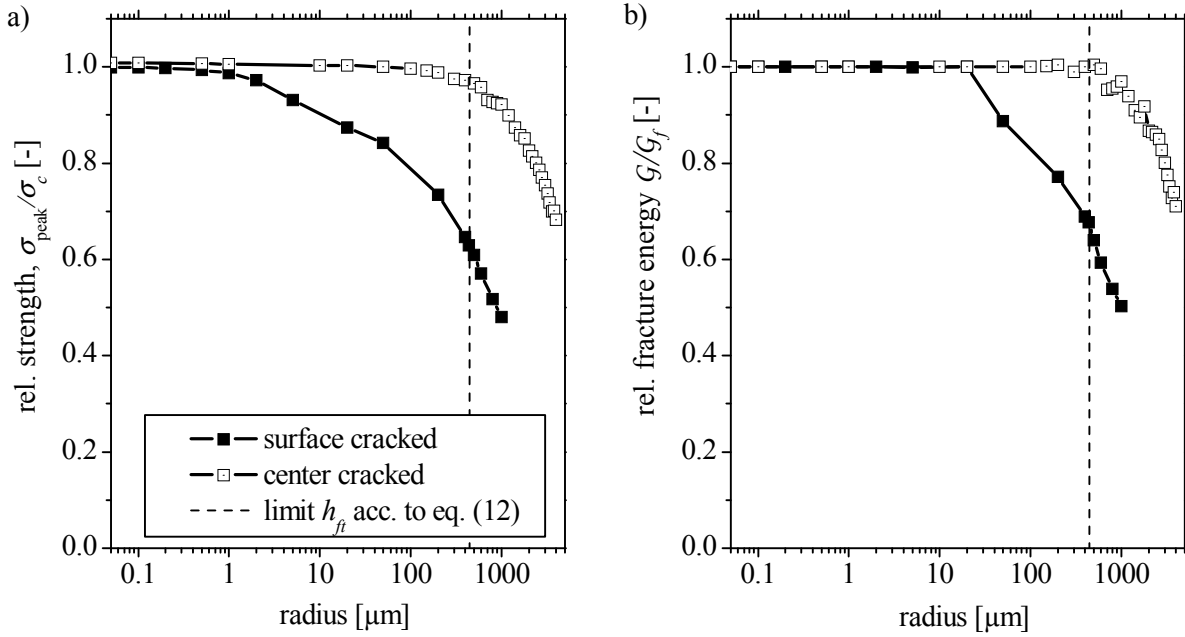
Fig. 5: Size effect of 3D surface cracked fibres compared to that of fibres with center crack (initially cracked area 10% of the specimen's cross section, threshold proposed by Gao et al. [8] is also shown; see Eq. (12)): a) Peak stress normalized by cohesive strength; b) Fracture energy, normalized by cohesive energy.

In summary, the applicability of the limit derived by Gao and co-workers depends crucially on the shape and orientation of the pre-existing defects (cracks). While for a fully symmetrical centre crack, the threshold (12) indeed defines a critical size for which a specimen can sustain flaws up to the ultimate strength of the material, that is not the case for surface cracked specimens. Clearly, real materials usually do neither show a fully symmetric crack nor a symmetric distribution of pre-existing cracks. For this reason, the limit proposed by Gao and co-workers has to be considered with care.

4. Failure of a ceramic reinforced polymer matrix composite

4.1. Model

Fibre breaking as analyzed in the previous subsection is not the only failure mechanism in fibre reinforced composites, but matrix cracking and fibre debonding are involved as well. In order to study the interaction between the complex material behaviour and the size effect, a series of geometrically equivalent RVEs is created with a regular arrangement of unidirectional short fibres. The loading is a prescribed displacement in longitudinal direction at the top surface, while the side surfaces are fixed (uniaxial straining). One of the fibres has a pre-crack at the surface with an area of 20% of the initial cross section area, seeFig. 6. The finite element mesh is also shown in the figure with symmetry conditions in the crack plane. Only one eighth of each fibre is contained in the model. Hence, mirroring the precracked fibre at the two symmetry planes leads to two cracks in the fibre. However, studies with a larger model containing the whole precracked fibre have predicted a similar response of the RVE. For this reason, the computationally more efficient smaller model is used. The cross section of RVEs ranges from $(0.1 \ \mu m)^2$ to $(1000 \ \mu m)^2$. The height is always three times the width of the RVE. The diameter of the fiber is 90% of the width and the aspect ratio of the fibre is 2.6, leading to a fibre volume ratio of approximately 57%.
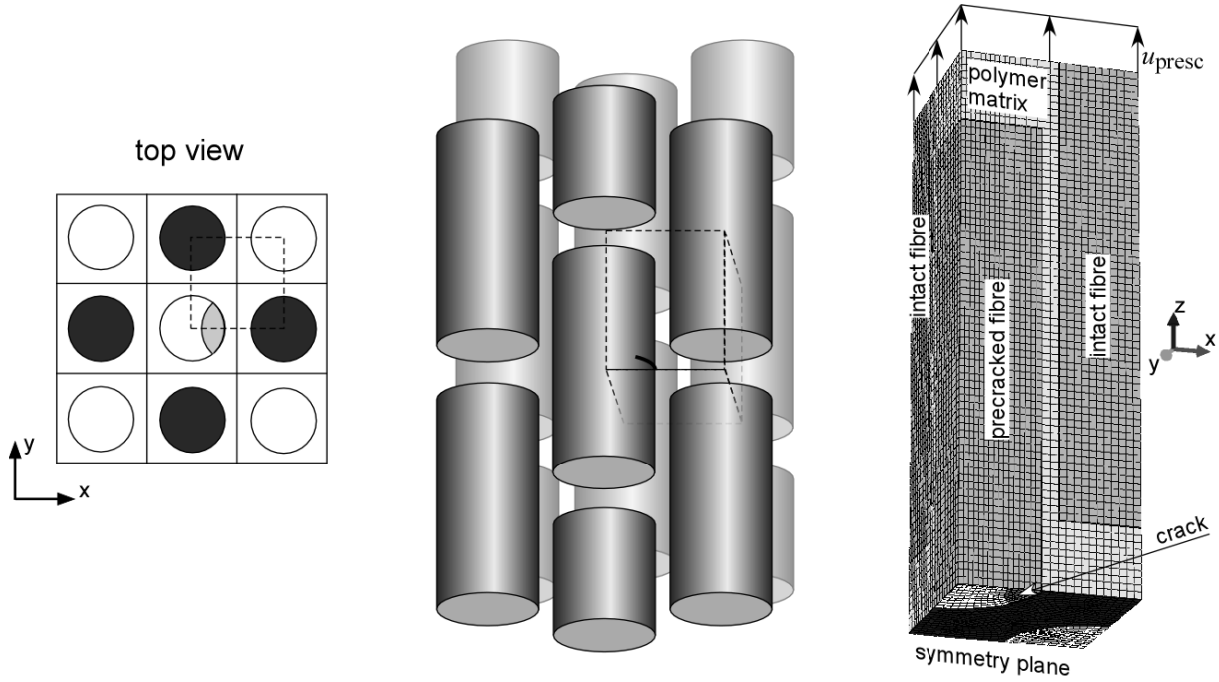
Fig. 6: Arrangement of unidirectional short fibres in the composite and finite element mesh of the representative volume element

Five different constitutive models are used: two for the elastic behaviour of the ceramic and the polymer, respectively, and three for the different failure properties of the fibre and the matrix (cohesive elements in the crack plane), and the cohesive elements for the interface between the constituents. The properties of the fibre are the same as presented in the previous section; the polymer matrix is also modelled by Hooke's law with material parameters taken from [25]. For the interface between the ceramic fibre and the polymer matrix, no specific values were given in [25]. Thus, reasonable assumptions were made for interface debonding. All parameters are summarized in Tab. 2.

Tab. 2: Material parameters characterizing the polymer and the interface between fibre and matrix.

Polymer		
Young's modulus	E_P	3,000 MPa
Poisson's ratio	ν_{PP}	0.33
Fracture energy	$\mathcal{G}_{f,P}$	120 J/m^2
Cohesive strength	$\sigma_{c,P}$	40 MPa
Cohesive elastic stiffness	$c_{,P}$	3,000 MPa/µm
Critical separation	$\delta_{c,P}$	6.0 µm
Interface between polymer and ceramic		
Fracture energy	$\mathcal{G}_{f,\text{int}}$	20 J/m^2
Cohesive strength	$\sigma_{c,\text{int}}$	40 MPa
Cohesive elastic stiffness	c_{int}	3,000 MPa/µm
Critical separation	$\delta_{c,\text{int}}$	1.0 µm

Two failure scenarios are possible under the applied loading conditions: fibre breaking as shown in Fig. 7a, and fibre debonding, see Fig. 7b. In addition to either mechanism, matrix cracking is necessary to tear the RVE completely apart. Since fibre debonding is highly dependent on the fabrication of the composite and the parameters are not fully reliable, the case of perfect bonding between polymer and ceramic is studied as well. In this case, the interface behaves purely elastic without any damage evolution and fibre breaking is a priori known to be the major failure mechanism.
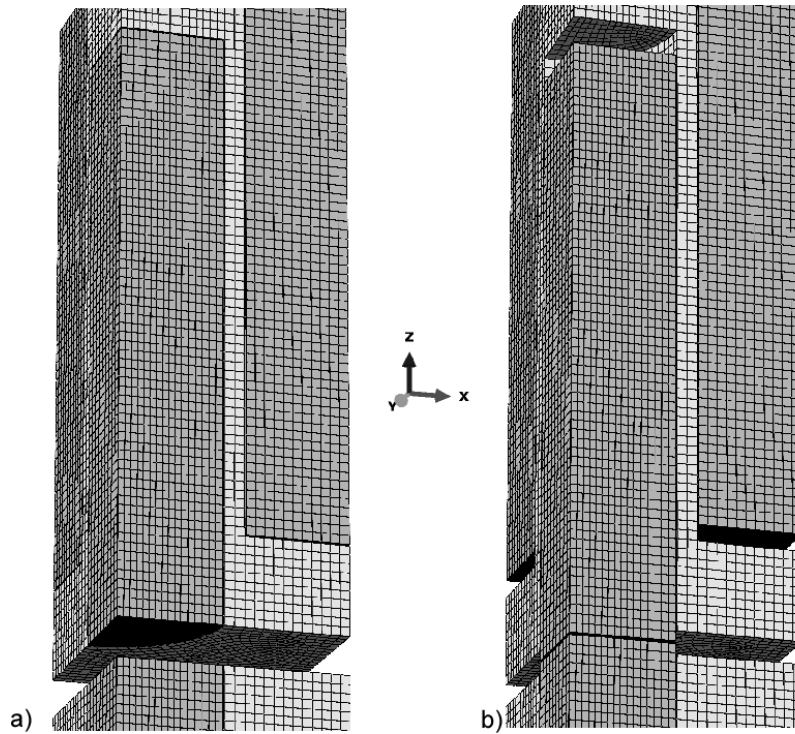
Fig. 7: Deformed mesh of the RVE (cohesive elements are removed); a) case 1 (mirrored at the crack plane) showing failure due to fibre breaking and matrix damage in the symmetry plane; c) case 2 (mirrored at the crack plane) showing failure due to debonding and matrix damage in the symmetry plane.

4.2. Results

The parameters given in Tab. 1 and 2 show that the critical separation at which the respective cohesive zone fails, is very large for the polymer matrix (6 µm), compared to approximately 1 µm for the fibre and the interface, i.e., the fibre fails before the matrix and the minimum applied displacement to tear the RVE apart is 6 µm. The average stress, computed as the force divided by the initial cross section area, is plotted versus the applied displacement for RVEs of two different sizes in Fig. 8. For the perfectly bonded interface, Fig. 8a, both RVE sizes behave very similar, showing three distinct regions: The peak stress is reached after the linear elastic regime, followed by a sharp decrease of the stress until the fibre is broken, since fibre failure occurs instantaneously. The gradual decrease in the third regime is due to matrix damage.

For a small RVE with fibre debonding (Fig. 8b), the mechanical behaviour is similar to that for the perfect bond (Fig. 8a). However, some interface debonding also occurs, which reduces the peak stress. For the larger RVE, debonding is the main failure mechanism. The slight decrease after the peak stress is caused by a gradual separation of the interface. After some debonding, matrix damage starts, which increases the rate of interface debonding and leads to a strong decrease in the resulting stress. Again, the last branch of the curves (after 2 µm displacement) is due to matrix cracking after complete debonding.
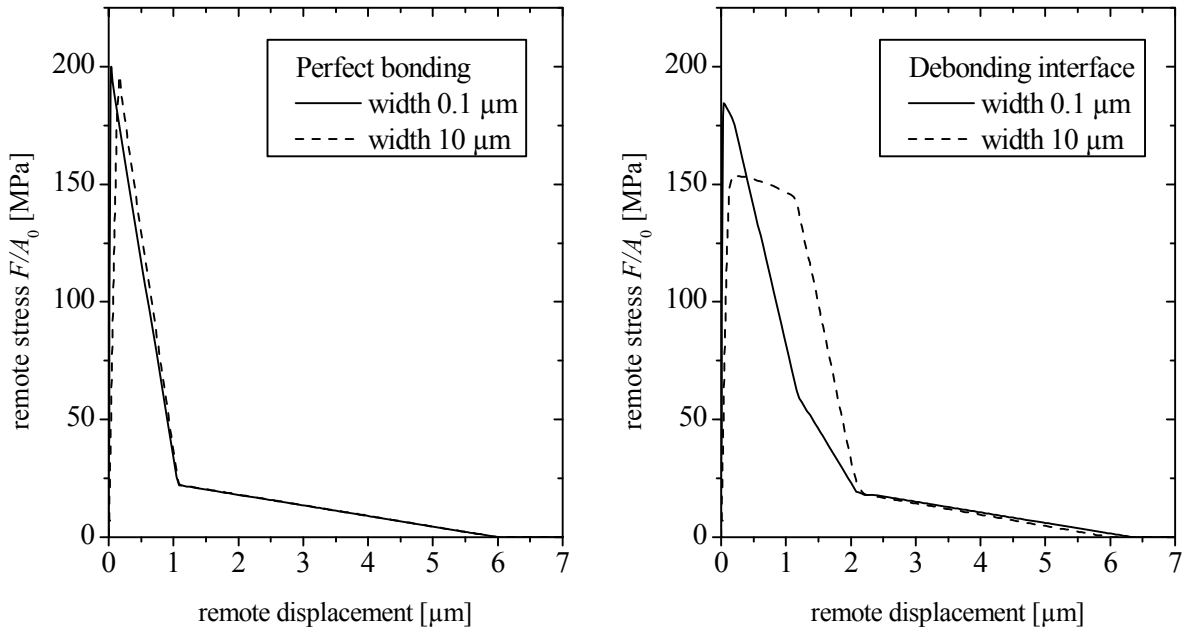
Fig. 8: Stress-displacement response of the RVE for selected sizes including perfectly bonded and debonding interface.

The effect of the RVE size on the peak stress and the fracture energy is shown in Fig. 9. The failure of small perfectly bonded RVEs can be assessed by a strength criterion, i.e. by the average strength of the fibre and the matrix. The peak stress decreases for larger RVE sizes. However, due to the suppressed bending of the fibre in the composite, the transition regime occurs for larger RVEs and is more pronounced than for a single fibre, cf. Fig. 5a. The fracture energy of the composite is hardly affected by the RVE size, see Fig. 9b.

As expected, for a debonding interface, the peak stress is always smaller than for the perfectly bonded interface. The peak stress decreases significantly when debonding is the main failure mechanism, i.e. for sizes of 10 μm and above, cf. Fig. 9a. In this case, the fracture energy, Fig. 9b, increases strongly due to high deformation capacity, which is caused by the gradual debonding of the interface.
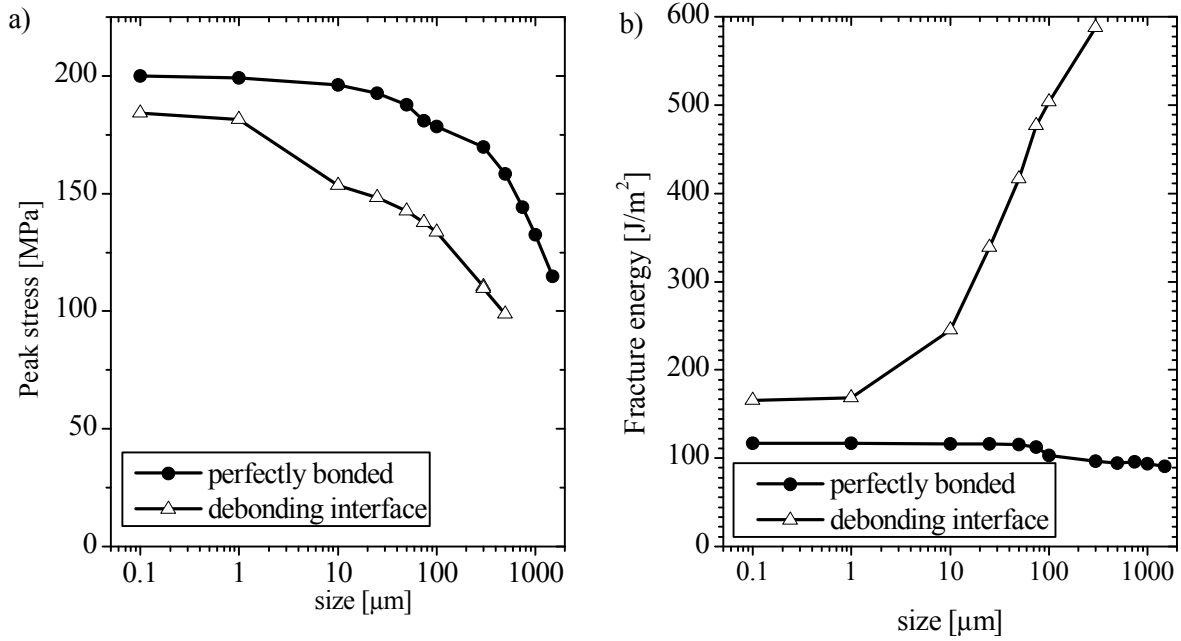
Fig. 9: Size effect of the 3D RVE (initial crack width 10%) for perfectly bonded and debonding fibres. a) averaged peak stress; b) averaged fracture energy.

4.3. Discussion

In classical continuum mechanics, all phenomena are size independent. However, due to the traction-separation law of the cohesive interface, a length scale is introduced in the model. Therefore, some effects depend on absolute sizes/displacements, while others are still size independent. This leads to a complex overall mechanical behaviour. For the analyzed fibre reinforced composite, the effect of debonding plays a major role. It reduces the strength, but increases simultaneously the fracture energy. Furthermore, the resulting size effect of the fracture energy is opposite to that of a single fibre, i.e., a large fibre dissipates much energy during the debonding process within fibre reinforced composites.

In addition, the competing failure mechanisms lead to a microstructural behaviour which is actually opposite to expectations from the single fibre. The smaller the fibre, the higher is its strength (Fig. 5); however, in the small RVE the single fibre fails by fibre breaking, while the larger RVE fails by fibre debonding. Certainly this transition depends on the material parameters chosen.

It should be mentioned that similar length scales as used here have been developed for fibre debonding, see e.g. [27]. However, the cricical length for debonding depends on the length of the fibre itself. Since the aspect ratio of the fibre geometry has been kept constant, a further study has not been performed here.

5. Conclusions

The size effect associated with material failure in short fibre reinforced composites has been investigated in the present paper by finite element simulations of representative volume elements (RVEs). Fibre cracking as well as debonding between fibre and matrix material was captured by adopting a fully three-dimensional cohesive zone model. The numerical results have shown a pronounced size effect of the RVE. The two sources identified for this effect are breaking and debonding of the fibres. For isolating these effects and for quantifying their influence, perfect bonding was numerically enforced. Furthermore, the size effect of the single fibres was separately investigated. In line with [2], it was shown that a single fibre reaches its theoretical strength, if the diameter is smaller than a certain threshold. This threshold depends strongly on the shape and orientation of the pre-existing micro-cracks. A centre crack, as assumed in the one-dimensional model advocated in [2], leads usually to an overestimation of the flaw tolerance. For this reason, a fully three-dimensional model is usually required.

In summary, the diameter of the fibres implicitly defines their relative strength. Analogously, by varying the length of the fibres, the fracture energy as well as the average strength related to fibre debonding can be modified. For this reason, an optimization of these two parameters (length and diameter

of the fibres) with respect to optimized macroscopic fracture properties of the fibre reinforced composites seems to be promising.

Acknowledgements

References

[1]   Kelly A, Zweben C (Eds.) Comprehensive Composite Materials. Elsevier Ltd, Oxford, 2000

[2]   Gao H. Application of fracture mechanics concepts to hierarchical biomechanics of bone and bone-like materials. *Int J Fract* 2006; 138:101-137.

[3]   Barthelat F, Rabiei R. Toughness amplification in natural composites. *J Mech Phys Solids* 2011; 59:829-840.

[4]   Bechtle S, Ang SF, Schneider GA. On the mechanical properties of hierarchically structured biological materials. *Biomaterials* 2010, 31:6378-6385.

[5]   Friedrich K, Karger-Kocsis J. Fractography and failure mechanisms of unfilled and fiber reinforced ssemi-crystalline thermoplastics. In: Roulis-Moloney AC (Ed.) Fractography and failure mechanisms of polymers and composites. Amsterdam: Elsevier Ltd.; 1989. 437-494.

[6]   Bennett JA, Young RJ. A strength based criterion for the prediction of stable fibre crack-bridging. *Compos Sci Tech* 2008;68:1282-1296.

[7]   Kang G-Z, Yang C, Zhang J-X. Tensile properties of randomly oriented short δ-Al2O3 fiber reinforced aluminium alloy composites. I. Microstructure characteristics, fracture mechanisms and strength prediction. *Compos A* 2002; 33:647-656.

[8]   Gao H, Chen S. Flaw tolerance in a thin strip under tension. *J. Appl. Mech.* 2005, 72 732-737.

[9]   Carpinteri A. Stability of fracturing process in r.c. beams. *J Struct. Engin* 1984; 110:544-558.

[10] Mishnaevsky Jr. L. Comutational Mesomechanics of Composites. John Wiley and Sons, London, 2007.

[11] Needleman A. A continuum model for void nucleation by inclusion debonding. J Appl Mech 1987; 54:525-531.

[12] Tvergaard V. Analysis of tensile properties for a whisker-reinforced metal-matrix composite. Acta Metall Mater 1990; 38:185-194.

[13] Tvergaard V. Model studies of fibre breakage and debonding in a metal reinforced by short fibres. *J Mech Phys Solids* 1993; 41:1309-1326.

[14] Brocks W, Scheider I. Prediction of crack path bifurcation under quasi-static loading by the cohesive model. *Struct Durab Health Monit* 2007; 3:69-80.

[15] Wang HW, Zhou HW, Mashnaevsky Jr. L, Brondsted P, Wand LN. Single fibre and multifibre unit cell analysis of strength and cracking of unidirectional composites. *Comp Mat Sci* 2009, 46:810-820.

[16] Peters PWM, Xia Z, Hemptenmacher J, Assler H. Influence of interfacial stress transfer on fatigue crack growth in SiC-fibre reinforced titanium alloys. *Compos A* 2001; 32:561-567.

[17] Dugdale, D. Yielding of steel sheets containing slits. *Journal of the Mechanics and Physics of Solids* 1960, 8 100-108.

[18] Barenblatt, G. The mathematical theory of equilibrium cracks in brittle fracture, *Advances in Applied Mechanics* 1962, 7, 55-129.

[19] Hillerborg A, Modeer M, Peterssen P. Analysis of crack formation and crack growth in concrete by means of fracture mechanics and finite elements. *Cement and Concrete Research* 1976, 6 773-782.

[20] Needleman A. A continuum model for void nucleation by inclusion debonding. *Journal of Applied Mechanics – Transactions of the ASCME* 1987, 54 525-531.

[21] Xu X, Needleman A. Void nucleation by inclusion debonding in a crystal matrix. *Modelling and Simulation in Materials Science and Engineering* 1993, 1 111-132.

[22] Park K, Paulino G, Roesler J. A unified potential-based cohesive model of mixed-mode fracture. *Journal of the Mechanics and Physics of Solids* 2009, 57 891-908.

[23] Mosler J, Scheider I. A thermodynamically and variationally consistent class of damage-type cohesive models. *Journal of the Mechanics and Physics of Solids* 2011, 59:1647-1668.

[24] Coleman B, Noll W. The thermodynamics of elastic materials with heat conduction and viscosity. *Archive for Rational Mechanics and Analysis* 1963, 13 167-178.

[25] Mosler J, Stankovic L, Radulovic R. Efficient modeling of localized material failure by means of a variationally consistent embedded strong discontinuity approach. *International Journal for Numerical Methods in Engineering* (2011), accepted.

[26] Radulovic R, Bruhns OT, Mosler J. Effective 3D failure simulations by combining the advantages of embedded strong discontinuity approaches and classical interface elements, *Eng. Fract. Mech.* 2010; 78:2470-2485.

[27] Chen B, Wu PD, Gao H. A characteristic length for stress transfer in the nanostructure of biological composites. Composites Science and Technology 2009; 69:1160-1164.